Near-infrared brightening around the periastron passages of the gamma-ray binary PSR B1259−63 / LS 2883

Akiko Kawachi,[1,]* Yuki Moritani,[2] Atsuo T. Okazaki,[3] Hiromi Yoshida,[1] and Kenta Suzuki[1]

[1]Department of Physics, School of Science, Tokai University, 4-1-1 Kita-kaname, Hiratsuka, Kanagawa 259-1292, Japan

[2]Kavli Institute for the Physics and Mathematics of the Universe (WPI), The University of Tokyo Institutes for Advanced Study, The University of Tokyo, 5-1-5 Kashiwanoha, Kashiwa, Chiba 277-8583, Japan

[3]Faculty of Engineering, Hokkai-Gakuen University, 4-1-40 Asahi-machi, Toyohira-ku, Sapporo, Hokkaido 062-8605, Japan

*E-mail: kawachi@tsc.u-tokai.ac.jp

Abstract

The binary of the pulsar PSR B1259−63 and the Be star LS 2883 has been observed at the 2010 and 2014 periastron passages in the near-infrared (NIR) bands using the IRSF/SIRIUS and SIRPOL. The light curves in the J-, H-, and K_s-bands are almost identical in these periastron passages. A flare starts no later than 10 days before periastron and the maximum brightening of about 0.1 mag is observed 12–17 days after periastron. The rising part of the light curve is steeper and reaches a peak slightly earlier in the K_s-band than in the other bands, thus a characteristic track appears on the NIR color–magnitude diagram. The time lag between the NIR light curves indicates that the variation in the Be circumstellar disk first occurs in an outer region. We propose that the initial rapid contraction followed by the gradual expansion of the disk is evoked by the rapidly changing tidal torque around periastron and the resultant change of the optically thick area causes the observed NIR light curves.

Key words: binaries: close — circumstellar matter — infrared: stars — pulsars: individual (PSR B1259–63) — stars: emission-line, Be

1 Introduction

PSR B1259−63 is a 48 ms period rotation-powered radio pulsar in a highly eccentric ($e = \sim 0.87$) and wide ($P_{\mathrm{orb}} = \sim 1236.72$ d) binary orbit (Shannon et al. 2014) with a Be star, LS 2883 (Johnston et al. 1992). LS 2883 has parameters corresponding to an O9.5Ve star whose mass M_* is $\sim 31\, M_\odot$ and radius R_* is $\sim 9.2\, R_\odot$ (Negueruela et al. 2011).

From the parallax measured by the long baseline radio interferometric observations, the distance to the binary is inferred to be $2.6^{+0.4}_{-0.3}$ kpc (Miller-Jones et al. 2018). The parallax was also provided using an astrometric fit of Gaia Data Release 3 (Lindegren et al. 2021) as 0.443 ± 0.013 mas, which corresponds to an inversion distance of 2.26 ± 0.07 kpc. However, Miller-Jones et al. (2018) points out that the semi-major axis of the orbit of LS 2883 is subtended by an order of 0.1 mas on the sky and the unmodelled orbital motion could significantly affect the fitted astrometric parameters. These distance values are consistent with the result of optical spectral analysis of LS 2883

(Negueruela et al. 2011) within the errors. The pulsed emission becomes undetectable around periastron (τ) during the period of about $\tau \pm 20$ d (Connors et al. 2002; Chernyakova et al. 2014). The absorption and the varying rotation and dispersion measures have shown that the Be circumstellar disk is inclined with respect to the orbital plane (Melatos et al. 1995) and the pulsar is assumed to pass behind the circumstellar disk around the periastron passage crossing the disk twice in each orbit, before and after periastron. The binary separation is about 0.9 au, i.e., $\sim 20 R_*$ (Negueruela et al. 2011) at its minimum and is $\sim 45 R_*$ around the ending of pulse eclipse, which implies that the Be-disk radius is larger than that (van Soelen et al. 2016).

The PSR B1259−63 system is the first binary to be detected in the TeV gamma-rays (Dubus 2013). The unpulsed X-ray emission is observed throughout the orbit (Hirayama et al. 1999), and radio (Johnston et al. 1999), X-ray (Kaspi et al. 1995; Chernyakova et al. 2006), GeV (Abdo et al. 2011; Caliandro et al. 2015), and TeV (Aharonian et al. 2005, 2009) flares have been detected around periastron. The multiwavelength observations have been repeatedly performed (e.g., Chernyakova et al. 2014; H.E.S.S. Collaboration 2020). The two-peak flare in the radio and the X-ray showed its first peak at $\sim \tau - 15$ d during the radio eclipse and the second at $\sim \tau + 18$ d, although the radio time profiles varied from orbit to orbit (Johnston et al. 2005). The X-ray spectrum is well described with a simple power-law with a photoelectric absorption and confirmed to extend up to a 100-keV energy region (Shaw et al. 2004). The broadband emission from the PSR B1259−63 system is produced by high-energy particles in the shocked pulsar wind. For the radio, X-ray, and possibly, TeV gamma-ray bands, the orbital light curves around the periastron can be interpreted as a result of the interaction of the pulsar wind with the stellar outflows of the Be star (e.g., Chernyakova et al. 2014). The GeV flare shows puzzling features which start approximately 30 d after periastron and have no counterpart in the other wavebands. The mechanism of the GeV flaring episode is still under discussion, with some theoretical interpretations considering either the unshocked pulsar wind or Doppler-boosted emission from shocked material and/or the enhanced photon field other than that which LS 2883 provides at the quiescent orbital phase (Khangulyan et al. 2012; Chernyakova et al. 2020; H.E.S.S. Collaboration 2020). Apart from these periastron events, an extended X-ray structure (clump) moving away from the binary was observed by a series of Chandra X-ray Observatory observations (Pavlov et al. 2015; Hare et al. 2019). The emission is considered to be a high-speed ejecta launched near periastron passage.

A Be star has a two-component extended atmosphere; a polar wind of low density and fast outflow emitting UV radiation and an equatorial circumstellar disk which is nearly Keplerian, consisting of a high-density plasma from which the optical emission lines and the IR excess arise (e.g., Porter & Rivinius 2003). Be disks in binary systems are considered to be subject to complex processes such as precession, warping, tidal deformation, and truncation (Rivinius et al. 2013) and effects of the pulsar wind add another complexity. Okazaki et al. (2010) and Takata et al. (2012) simulated the PSR B1259−63 system using a framework of a three-dimensional smoothed particle hydrodynamics (SPH) method. In their simulations, the pulsar wind disturbs the circumstellar environment around periastron. The contact surface between the pulsar and stellar outflows changes according to the density and geometrical parameters of the disk. The disk under the influence of the tidal torque also deforms density distribution and effective radial size according to the orbital phase.

In order to understand the orbital perturbation on the circumstellar disk of LS 2883, which can also be used as a probe to constrain the high-energy emission mechanism of the binary, we report the observation results of the LS 2883 in the NIR band around the periastron passage.

2 Observations and analysis

The monitoring observations of the binary were performed around the 2010 and 2014 periastron passages (including the periastron τ of MJD 55544.69 and 56781.42, respectively) for about a month in each orbital cycle with some observations in the quiescent phase (from $\tau - 300$ d to $\tau - 85$ d in 2010).

All the observations used the IRSF (InfraRed Survey Facility) 1.4 m telescope located at the Sutherland station of the South African Astronomical Observatory (SAAO) with the three-channel infrared camera, SIRIUS (Simultaneous InfraRed Imager for Unbiased Survey: Nagayama et al. 2003) mounted on the Cassegrain focus of the telescope. The SIRIUS camera is equipped with the two dichroic filters and the three 1024 × 1024 HgCdTe detectors (HAWAII arrays). It offers three J (1.25 ± 0.085 μm), H (1.63 ± 0.15 μm), and K_s (2.14 ± 0.16 μm) images simultaneously with a field of view of 7$.\!\!^{\prime}$7 × 7$.\!\!^{\prime}$7 and a pixel scale of 0$.\!\!^{\prime\prime}$45.

We performed 156 observations during 25 nights in the 2010-cycle and 137 observations in 33 nights in the 2014-cycle. The typical seeing was four-pixel for the H-band; however, less photometric observations were included. A single image is typically combined with 25 dithered frames of 3 to 10 s exposures. For most of the 2010 observations (20 of the 25 nights), the single beam polarimeter SIRPOL (SIRius POLarimetry mode) was utilized. SIRPOL consists of a half-wave plate rotator unit and a high-efficiency wire-grid polarizer located upstream of the camera (Kandori
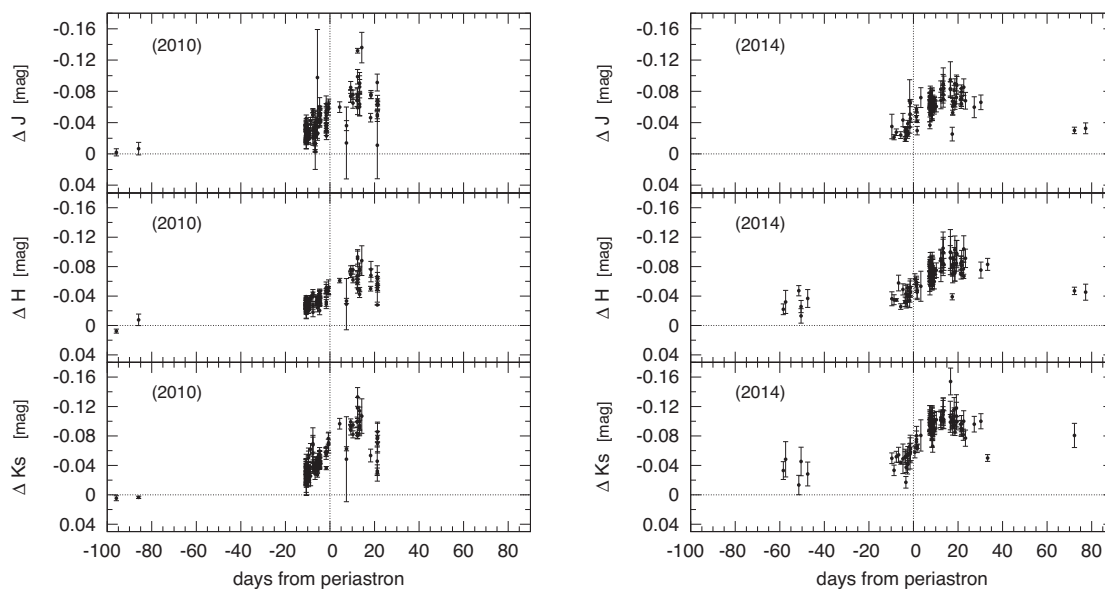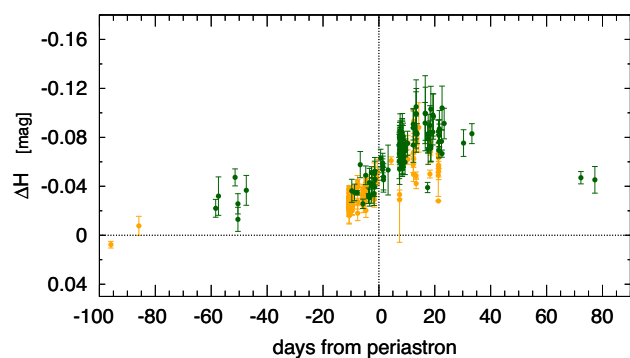
Fig. 1. *J*-, *H*-, and *K*$_s$-bands light curves as a function of days from periastron, for the 2010 cycle (left) and the 2014 cycle (right), respectively. We use the observation in the quiescent phase ($\tau - 199$ d in 2010) as the common reference to the light curves in both orbital cycles. (see the text).

et al. [2006]). The typical accuracy of the polarization degree δP is ~0.3% depending on the stability of the sky.

The primary data reduction has been carried out with the standard pipeline software for SIRIUS and SIRPOL including dark-subtraction, flat-fielding, self-sky subtraction, and combining the dithered frames.[1] The detectors of SIRIUS keep a good linearity (< 1%) up to ~10000 ADU but saturate at ~25000 ADU, e.g., for the K_s-band (Narita et al. [2014]). Aperture photometry is followed using the IRAF APPHOT task with the aperture sizes adjusted using the FWHM values of multiple stars in the respective image. For the SIPOL data, the Stokes *I*-images are used for the photometric light curve. The SIRPOL *I*-images and the SIRIUS images without the polarimeter taken in a short time interval are compared and the photometry results of these images are confirmed to agree well.

Differential photometry with the multiple reference stars are calculated and the light curves in reference to a quiescent phase observation ($\tau - 199$ d) are deduced. The standard error of the zero point of instrumental magnitude is adopted in the error of each observation, together with the statistical errors. The deviations of the photometric results of a set of 20–30 sequential observations in a good-conditioned night are about 0.01 mag. The independent analysis of the observation at MJD = 55549 ($\tau + 4$ d) in the 2010 cycle (van Soelen et al. [2012]) is consistent within the errors.

Fig. 2. *H*-band light curves in the two orbital cycles are overplotted with different colors; the 2010 cycle (orange) and the 2014 cycle (green). (Color online)

3 Results

3.1 Light curves

The differential light curves in the *J*-, *H*-, and K_s-bands are shown in figure 1 as a function of days from the periastron. In the 2014 orbital cycle, some data points of the *J* and K_s bands are missing due to the moderate data condition. The flares of about 0.1 mag emerged in all the three bands around periastron similarly in both of the orbital cycles. The flares reached maximum brightness about $\tau + 12$ d and gradually decayed afterwards. In 2014, the brightness was nearly back to the level in the quiescent phase at $\tau + 70$ d. The brightening episode might have started before our first observation in the periastron passage ($\tau \sim -10$ d) but the significance is not high considering the errors. In figure 2, the *H*-band light curves for the 2010 and 2014 orbital cycles are overlapped. The flares of the two cycles

---

[1] The pipelines are scripts based on IRAF command procedures ⟨https://sourceforge.net/projects/irsfsoftware/⟩.

are almost identical except for the slight differences in the timing of the maximum brightness and in the decay time scale.

3.2 Color–magnitude diagrams

The infrared color $(H - K_s)$ and the H-band magnitude of the observation data are plotted as diagrams for each orbital cycle (figure 3). The infrared color is calculated by taking the differential of the same reference observation in the analysis. The temporal changes of the flares in the J and H bands are about the same and the $(J - H)$ color values are approximately constant over the observed phase. In these diagrams, different colors correspond to different orbital phases. The diagrams for the two orbital cycles exhibit a similar phase-dependent behavior.

The infrared color goes redder with increase in the brightness until $\sim \tau + 10$ d then starts to turn blue while the brightening still continues. At the flux maxima in the H band ($\sim \tau + 18$ d), the color is almost back to that in the period prior to the flare. This two-step color change is caused by the difference in the temporal features of the brightening in the K_s and H bands. The brightness in the K_s band increases more rapidly than in the H band, which makes the infrared color redder at first, and the K_s-band flux has a peak a few days earlier than does the H-band flux. However, the flux increase of the H band gradually catches up with that of the K_s band, which turns blue, forming the upper branch of the brightening track. The infrared color becomes redder again as the flare decays. The decay track in the diagram coincides with the brightening track, yet the kink phase cannot clearly be located due to the lack of the observations.

4 Discussion

4.1 No association with the radio synchrotron flares

The brightening in the NIR band started no later than 10 days prior to the periastron passage, the timing of which is similar to that of the first flare in the unpulsed radio and X-ray emissions. The flux of 1.4–8.4 GHz increased from the detection limit to several 10 mJy. Fitted by a power-law function of the form $S_\nu = C\nu^\alpha$, the radio spectral index α is about -0.6 (Johnston et al. 2005). If this simple power-law form is extrapolated from the radio to the NIR band, the contribution of this flare would be $\sim 10^{-2}$ mJy. This flux is about four orders of magnitude smaller than the LS 2883 NIR emission composed of the stellar atmosphere and the circumstellar disk (van Soelen & Meintjes 2011), by which the total flux would vary only 10^{-4} magnitude. We can, thus, rule out the possibility of the association of the radio synchrotron flare with the observed NIR brightening of 0.1 mag of this work.

4.2 Be-disk evolution by the tidal interactions and its effect on the NIR emissions

The IR continuum excess of Be stars are interpreted as free–free and free–bound emissions of the circumstellar disk (Porter & Rivinius 2003). The IR emissivity of an optically thin disk increases/decreases with increase/decrease in the local density. On the other hand, for optically thick disks, the disk luminosity is roughly proportional to the area where the disk is optically thick to the wavelength in consideration. The radius of the optically thick region is larger for a longer wavelength. For more details see figures 2 and 7 of Rivinius, Carciofi, and Martayan (2013).

The tidal effect of the neutron star on the Be disk is enhanced around periastron in eccentric Be binaries. Okazaki et al. (2002) has studied the orbital modulation of the Be disk structure as well as the long-term disk evolution under the influence of the neutron star using a three-dimensional SPH code. In snapshots taken at several orbital phases [figures 10 and 11 of Okazaki et al. (2002)], the disk starts to contract just before periastron by the tidal torque from the neutron star and then expands as the neutron star moves away from periastron. Thus the effective disk radius modulates around the mean value. Throughout this period of strong tidal interaction, the disk is deformed. After repeating contraction and expansion a few more times, the disk becomes almost axisymmetric and starts to restore its radius slowly by viscous diffusion. Although the strength of the interaction is dependent on the inclination angle of the Be-disk to the orbital plane, this variation of the disk structure, in density distribution and in effective radius, is expected to be observed around the binary periastron passage.

Figure 4 shows the optical spectroscopic monitoring results of the PSR B1259−63 binary at the 2014 periastron passage (van Soelen et al. 2016) together with the H-band differential light curve and NIR color variation of this work. The He I (λ 6678) line shows a consistent double-peak structure but showed variation in the strength. The constraint on the emission location of He I (figure 4b) is derived as in van Soelen et al. (2016) from the peak separation of the lines assuming a Keplerian disk. They use $v \sin i = 260 \pm 15$ km s^{-1} (Negueruela et al. 2011) in the calculation. The He I location moves outwards after periastron and reaches a maximum radius around $\tau + 14$ d when the NIR bands were brightest (figure 4c).
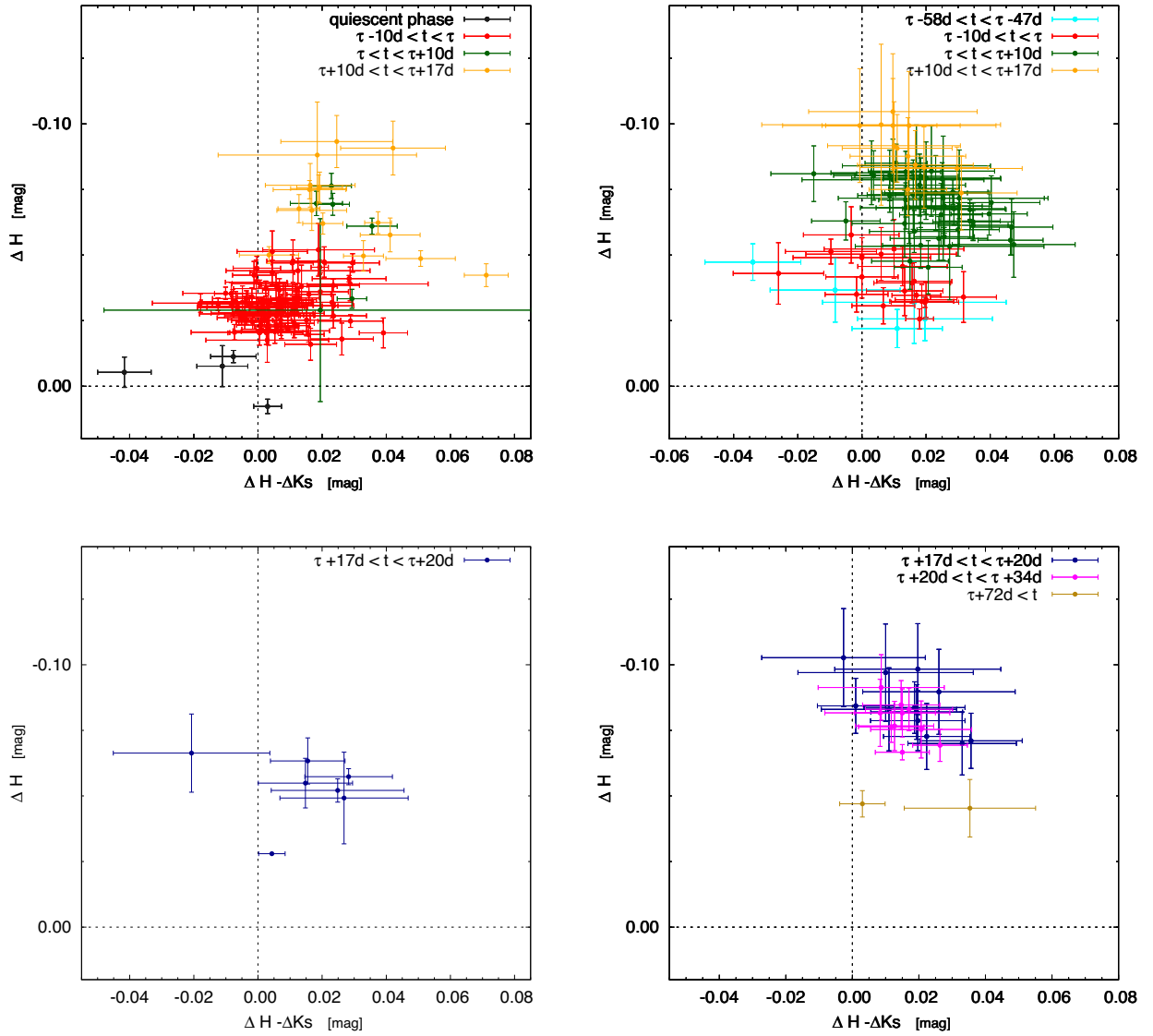
Fig. 3. Diagrams of the relative NIR color ($\Delta H - \Delta K_s$) and the H-band differential magnitude ΔH are shown for the periods of brightening (top) and decay (bottom) in the 2010 cycle (left) and the 2014 cycle (right). Different colors of the points correspond to different orbital phases. (Color online)

The movement of the location of the He I emission can be interpreted by the expansion of the disk after the contraction in the inner part evoked by the tidal torque. Assuming the LS 2883 disk is optically thick, the expansion of the disk leads to an increase of the optically thick area and hence of the NIR flux. Therefore it is no coincidence that the NIR flares are observed when the He I emission location moves outwards. The increase of the equivalent width of Hα line (Chernyakova et al. 2015, 2020) is qualitatively consistent with this interpretation. Here, we note that it is rather natural that the initial tidal contraction is not seen in the light curve of the Hα line, given that the line mainly arises from the outer part of the disk, where the pulsar wind has a much stronger effect than the tidal torque. The He I location might have shifted inwards around $\tau - 20$ d as a sign of

disk contraction, although the shift is not significant given the size of the error bars. There is also a hint of oscillation around $\tau + 40$ d, which is not statistically significant either. V/R, the ratio of the height of the V component to that of the R component, of the double-peaked He I line has local maxima around $\tau - 20$ d and $\tau + 40$ d. This variation suggests that the strong disk deformation occurs around these dates, which are close to the timings of the first disk-crossing of the pulsar and the GeV flare, respectively. Unfortunately, NIR observations are missing for these periods.

As described in section 3, the observed kinked pattern on the NIR color–magnitude diagram is the result of the different timings of brightening between the H and K_s bands. The earlier response in the K_s band indicates that the disk variation starts in the outer region. In the
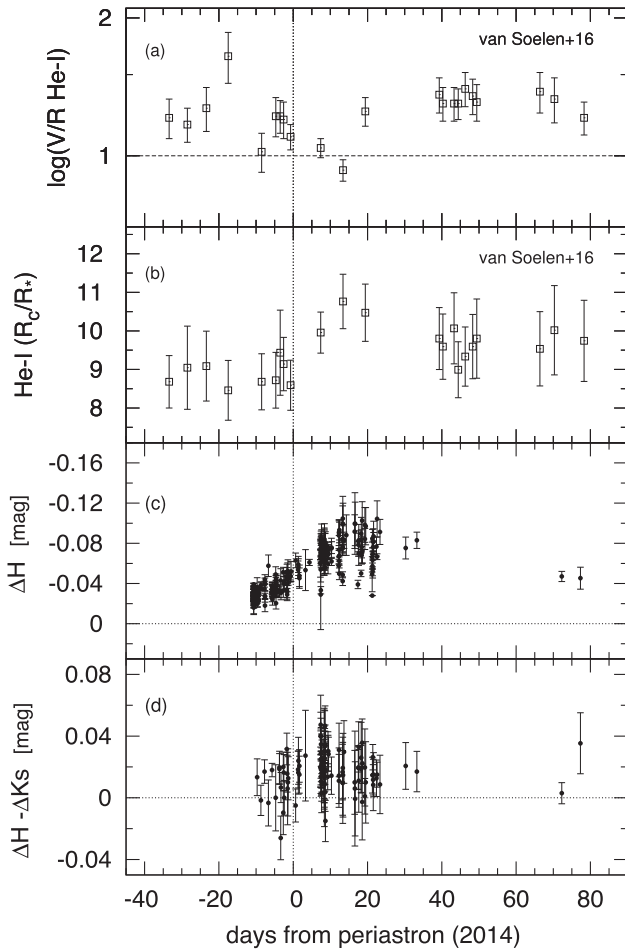
Fig. 4. Variations in the He I emission (van Soelen et al. 2016) in the 2014 orbital cycle of the binary are compared with the NIR observations of this work. (a) VR ratio of the He I line emission shown in log scale, (b) location of the He I emission R_C in units of stellar radius R_*, (c) differential light curve in the H-band, ΔH and (d) relative NIR color variation ($\Delta H - \Delta K_s$).

PSR B1259−63/LS 2883 binary, the Be disk expands first in the outer region and then in the inner region.

The destruction of the LS 2883 Be disk has been discussed to explain the trigger of the GeV flaring (Chernyakova et al. 2015) or the extended X-ray ejecta (Pavlov et al. 2015). Such an event is most likely to occur in the outermost region of the disk, where the pulsar wind effect is strongest. On the other hand, the NIR variability studied in this work arises from an inner intact region and cannot be directly connected with the disk-destruction episodes.

Panoglou et al. (2016) calculated light curves for $\lambda = 0.5\,\mu$m, $3\,\mu$m, and 1 mm using the SPH simulation data of a Be-star binary. Their calculation shows the brightening occurs after periastron at different timings for different wavelengths. However, because of the simulation setting where the compact object moves within the disk from well

before periastron, a direct comparison with our results is difficult.

5 Conclusions

The NIR monitoring of PSR B1259−63 was performed around the 2010 and 2014 periastron passages. Almost identical flaring light curves with the maximum brightening of about 0.1 mag in the J, H, and K_s bands were observed in both cycles. Associated with the flaring event, a characteristic kinked pattern appeared on the NIR color–magnitude diagram. This phase-dependent movement on the diagram is due to the fact that the K_s band brightens faster than the other two bands, which indicates that the variation in the Be circumstellar disk is first excited in the outer region and then propagates inwards. The observed NIR variability is likely caused by the Be disk expansion and the resultant increase of optically thick areas, which is evoked by the tidal interaction with the pulsar around periastron.

Funding

References

Abdo, A. A., et al. 2011, ApJ, 736, L11

Aharonian, F., et al. 2005, A&A, 442, 1

Aharonian, F., et al. 2009, A&A, 507, 389

Caliandro, G. A., Cheung, C. C., Li, J., Scargle, J. D., Torres, D. F., Wood, K. S., & Chernyakova, M. 2015, ApJ, 811, 68

Chernyakova, M., Neronov, A., Lutovinov, A., Rodriguez, J., & Johnston, S. 2006, MNRAS, 367, 1201

Chernyakova, M., et al. 2014, MNRAS, 439, 432

Chernyakova, M., et al. 2015, MNRAS, 454, 1358

Chernyakova, M., Malyshev, D., Mc Keague, S., van Soelen, B., Marais, J. P., Martin-Carrillo, A., & Murphy, D. 2020, MNRAS, 497, 648

Connors, T. W., Johnston, S., Manchester, R. N., & McConnell, D. 2002, MNRAS, 336, 1201

Dubus, G. 2013, A&AR, 21, 64

H. E. S. S. Collaboration, 2020, A&A, 633, A102

Hare, J., Kargaltsev, O., Pavlov, G., & Beniamini, P. 2019, ApJ, 882, 74

Hirayama, M., Cominsky, L. R., Kaspi, V. M., Nagase, F., Tavani, M., Kawai, N., & Grove, J. E. 1999, ApJ, 521, 718

Johnston, S., Ball, L., Wang, N., & Manchester, R. N. 2005, MNRAS, 358, 1069

Johnston, S., Manchester, R. N., Lyne, A. G., Bailes, M., Kaspi, V. M., Qiao, G., & D'Amico, N. 1992, ApJ, 387, L37

Johnston, S., Manchester, R. N., McConnell, D., & Campbell-Wilson, D. 1999, MNRAS, 302, 277

Kandori, R., et al. 2006, Proc. SPIE, 6269, 626951

Kaspi, V. M., Tavani, M., Nagase, F., Hirayama, M., Hoshino, M., Aoki, T., Kawai, N., & Arons, J. 1995, ApJ, 453, 424

Khangulyan, D., Aharonian, F. A., Bogovalov, S. V., & Ribó, M. 2012, ApJ, 752, L17

Lindegren, L., et al. 2021, A&A, 649, A2

Melatos, A., Johnston, S., & Melrose, D. B. 1995, MNRAS, 275, 381

Miller-Jones, J. C. A., et al. 2018, MNRAS, 479, 4849

Nagayama, T., et al. 2003, Proc. SPIE, 4841, 459

Narita, N., Nagayama, T., Suenaga, T., Fukui, A., Ikoma, M., Nakajima, Y., Nishiyama, S., & Tamura, M. 2013, PASJ, 65, 27

Negueruela, I., Ribó, M., Herrero, A., Lorenzo, J., Khangulyan, D., & Aharonian, F. A. 2011, ApJ, 732, L11

Okazaki, A. T., Bate, M. R., Ogilvie, G. I., & Pringle, J. E. 2002, MNRAS, 337, 967

Okazaki, A. T., Nagataki, S., Naito, T., Kawachi, A., Hayasaki, K., Owocki, S. P., & Takata, J. 2010, PASJ, 63, 898

Panoglou, D., Carciofi, A. C., Vieira, R. G., Cyr, I. H., Jones, C. E., Okazaki, A. T., & Rivinius, T. 2016, MNRAS, 461, 2616

Pavlov, G. G., Hare, J., Kargaltsev, O., Rangelov, B., & Durant, M. 2015, ApJ, 806, 192

Porter, J. M., & Rivinius, T. 2003, PASP, 115, 1153

Rivinius, T., Carciofi, A. C., & Martayan, C. 2013, A&AR, 21, 69

Shannon, R. M., Johnston, S., & Manchester, R. N. 2014, MNRAS, 437, 3255

Shaw, S. E., Chernyakova, M., Rodriguez, J., Walter, R., Kretschmar, P., & Mereghetti, S. 2004, A&A, 426, L33

Takata, J., et al. 2012, ApJ, 750, 70

van Soelen, B., & Meintjes, P. J. 2011, MNRAS, 412, 1721

van Soelen, B., Meintjes, P. J., Odendaal, A., & Townsend, L. J. 2012, MNRAS, 426, 3135

van Soelen, B., Väisänen, P., Odendaal, A., Klindt, L., Sushch, I., & Meintjes, P. J. 2016, MNRAS, 455, 3674